Towards acoustic microscopy at the nanoscale by coupling atomic force microscopy with picosecond ultrasonics

R. Delalande,[*] D. Garcia-Sanchez, and L. Belliard[†]
Sorbonne Université, CNRS UMR 7588, Institut des NanoSciences de Paris, INSP, F-75005 Paris, France

(Received 2 May 2022; revised 21 December 2022; accepted 19 January 2023; published 10 February 2023)

Acoustic imaging techniques are powerful, nondestructive tools used to perform elastic imaging of systems. Acoustic imaging techniques have a large variety of applications in both industrial and fundamental research. Acoustic wave generation in the GHz range using picosecond acoustics has enabled the development of elastic images with nanometric in-depth resolution. However, the spatial lateral resolution for this imaging technique is limited by the laser spot size, which cannot be reduced below a couple hundred nanometers due to light diffraction. In this paper, we report the results from an approach in which we couple time-resolved pump-probe spectroscopy and atomic force microscopy. We generate GHz waves directly into an AFM probe from the top of the probe. Acoustic transmission from the probe to the sample is also achieved, which paves the way to perform subsurface imaging. Due to the nanometric radius size of the commercial tip, acoustic imaging with an improved lateral resolution could be achieved. These results are an encouraging step toward the development of a new acoustic microscopy technique.

DOI: 10.1103/PhysRevB.107.085409

I. INTRODUCTION

Since picosecond acoustics was developed by Thomsen *et al.* [1,2], time-resolved pump-probe spectroscopy has proven to be a very effective way to probe and image nanoscale elastic properties of a wide variety of materials. Employed in both industrial and fundamental research, it has recently been used to perform elasticity imaging of various systems such as biological cells [3–10] and polycrystalline materials [11–13]. The generation of acoustic waves with frequencies up to a couple hundred GHz enables achievement of very good in-depth resolution [14]. However, the spatial resolution is limited to a few hundred nanometers because the laser spot size is limited by light diffraction. Despite this boundary, several techniques have been proposed to improve the lateral resolution, such as using acoustic lenses [15,16] and working in the near field [17,18]. The latter enables a lateral resolution of 50 nm. Optical super-resolution imaging has also been investigated through various devices using solid immersion lenses [19–21], nanoparticles [22], and near-field probes [23]. In order to perform elastic imaging, another approach is to use acoustic nanosources with characteristic sizes smaller than the typical laser spot. The study of vibrations of nanoparticles, notably by time-resolved spectroscopy [24–26], has highlighted a strong coupling between a nanoparticle and its environment, especially with its substrate [27–29]. Several studies have taken advantage of this coupling in order to probe properties at the nanoscale [30] and to use nanoparticles as acoustic nanosources [31–35]. Although the emission of a controlled frequency acoustic field in the GHz range has been proven for several shapes and materials, these sources are not adapted to the development of acoustic microscopy at the nanometric scale. Indeed, the ability to manipulate a nanoparticle on a surface is limited and its position is typically poorly controlled. Another approach consists of performing elastic imaging at the nanoscale by coupling acoustics and atomic force microscopes (AFM) [36–38]. The possibility of performing 3D nondestructive subsurface imaging is of a great interest [39,40]. Most of these techniques, such as ultrasonic force microscopy [40], atomic force acoustic microscopy [41,42], and heterodyne force microscopy [43,44], use piezoelectric actuators to excite the sample, the cantilever, or both items. However, the use of piezoelectric crystals limits the frequency range that can be investigated to an upper limit of a couple of GHz. This is why recent developments involve coupling AFM with picosecond acoustics [45,46].

In this paper, we propose an approach of coupling AFM and picosecond ultrasonics. Here, the generation of acoustic waves and their detection are carried out at the free surface of the cantilever. The tip acts as a confinement system that is used to probe and excite the sample. Acoustic propagation in a conical silicon tip is first investigated both experimentally and numerically. The sensitivity of the acoustic field detected at the back of the cantilever to a sample is proven, and the first results of impedance surface imaging of a structured sample are demonstrated in contact mode. Acoustic transmission through the AFM probe to the sample in contact is also highlighted, which paves the way for 3D acoustic imaging at the nanoscale. This transmission is also confirmed numerically.

II. EXPERIMENTAL SETUP

During this study, two experimental setups were used. The schematics of those setups are introduced in Fig. 1. Both

[*]Present address: Laboratoire d'Acoustique de l'Université du Mans (LAUM), UMR 6613, Institut d'Acoustique - Graduate School (IA-GS), CNRS, Le Mans Université, France.
[†]Corresponding author: belliard@insp.upmc.fr

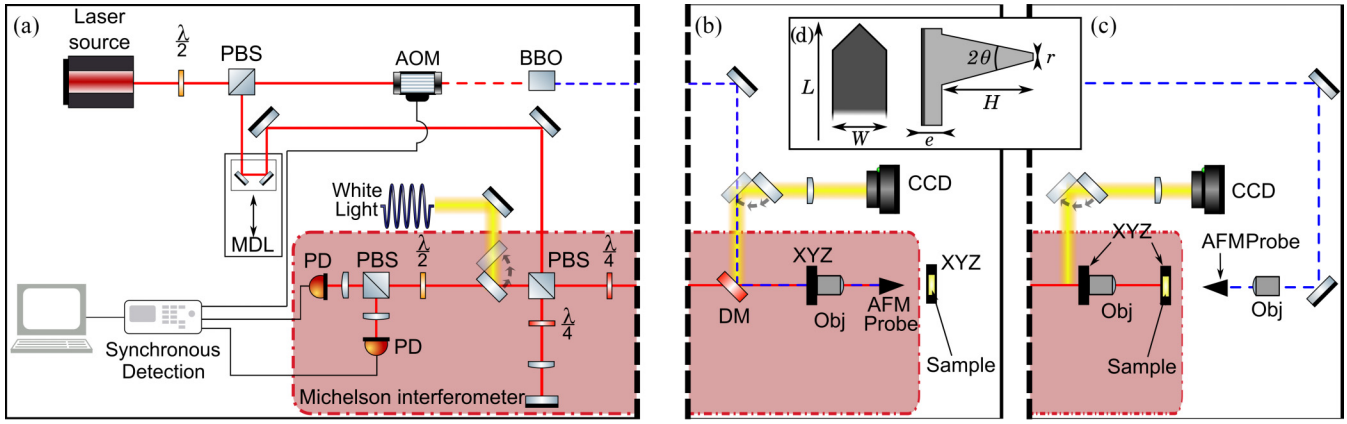

FIG. 1. (a) Left side of the experimental setup in both configurations. (b) Right side in reflection geometry. (c) Right side in transmission geometry. (d) Drawing of the top and side profile of the AFM probe. PSB: Polarizing beam splitter. AOM: Acousto-optic modulator. BBO: Beta barium borate crystal. MDL: Mechanical delay line. PD: Photodiode. DM: Dichroic mirror. Obj: Objective. XYZ: Piezoelectric stage. CCD: Camera. $\lambda/2$ and $\lambda/4$: Half and quarter wave plate.

are based on a mode-locked Ti:sapphire (MAI-TAI Spectra) laser source operated at 800 nm with a pulse duration below 100 fs at the laser output and a repetition rate of 78.8 MHz. Synchronous detection is performed by modulating the pump beam at 1.8 MHz using an acousto-optic modulator. In both configurations we performed a two-color pump-probe experiment by doubling the frequency of the pump beam using a nonlinear crystal made of beta barium borate resulting in a pump wavelength of 400 nm. The probe beam wavelength is kept at 800 nm.

In the first configuration, Figs. 1(a) and 1(b), both pump and probe laser beams are aligned using a dichroic mirror and focused on the back of an AFM probe using an objective with a numerical aperture (NA) of 0.50 and a 50× magnification fixed on a piezoelectric stage. The AFM probe is installed on a fixed support while the sample is fixed on a second piezoelectric stage in order to control its position with respect to the AFM tip and to put the sample and the probe in contact. The reflected probe beam is measured with two avalanche photodetectors ADP from ThorLabs. A Michelson interferometer is used to improve the sensitivity to the surface normal displacement [47].

In the second setup, Figs. 1(a) and 1(c), the pump beam is still focused on the AFM probe using the same objective; however the probe beam is focused on the back of a sample using an objective with a NA of 0.42 and a 50× magnification. The two beams can be aligned and the probe objective is mounted on a piezoelectric plate allowing the mapping of the acoustic field around the generation epicenter. More details can be found in [32]. The powers of the pump and probe beams are limited to 1 and 10 mW, respectively, in order to work in the photoelastic regime and avoid ablation.

The AFM probes used in this study are commercially available CT130 probes made of monocrystalline highly doped *n*-silicon. The main characteristics of these probes are given in Table I and Fig. 1(d). The cantilever is along the $[1\bar{1}0]$ axis of the crystal while the tip is along the [100] axis. The AFM probe has been purchased with a nanometric aluminum layer covering the back surface. This thin film plays the role of an optical transducer, enhancing both the generation and the detection processes. Its good bonding is confirmed by the absence of strong oscillations in the transient signal, right after the electronic response. Those oscillations would have been caused by acoustic waves bouncing back and forth in this metallic layer instead of being transmitted to the Si [48].

In the present study, the measurements were not done with a conventional microscope with a feedback loop. However, the acoustic measurements require synchronous detection. Therefore, no disturbance associated with tilt measurements, which typically use continuous diode, are expected.

III. RESULTS AND DISCUSSION

A. Acoustic propagation within an AFM probe

First, the acoustic propagation within an AFM probe has been investigated. A scanning electron microscopy (SEM) image of an AFM probe is shown in Fig. 2(c). Both pump and probe beams are focused on the cantilever far from the position of the tip, as shown in Fig. 2(b). The relative variation of the reflectivity measured on the aluminum layer is shown in Fig. 2(a). An important variation of the signal is observed at 0 ps which is caused by the absorption of the pump beam and the temperature increase of the electron gas in the Al. The slowly increasing background is due to the cooling of the metallic layer following the thermalization of the lattice

TABLE I. Specifications of the used AFM probes.

Parameter (Unit)	Nominal value	Range
Cantilever:		
Spring constant k (Nm^{-1})	6	[2; 10]
Length L (μm)	125	[115; 135]
Width W (μm)	42	[40; 45]
Thickness d (μm)	1.7	[1.0; 3.0]
Tip:		
Height H (μm)	15	[12.5; 17.5]
Cone angle θ (°)	30	
Radius r (nm)	10	

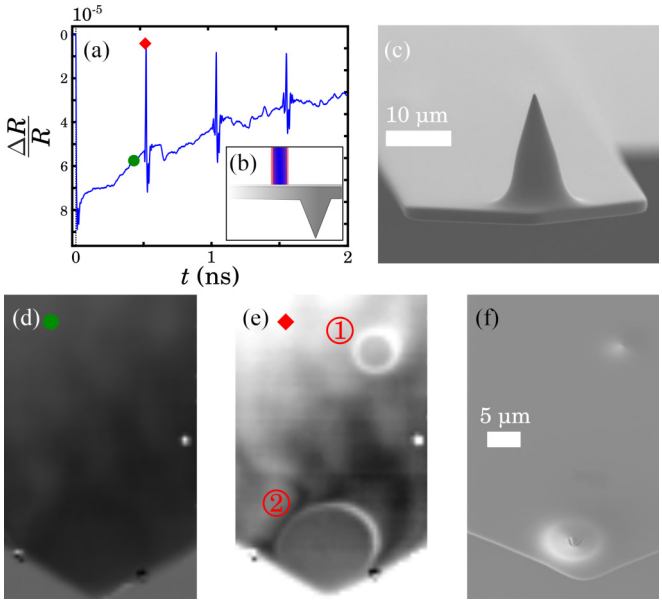

FIG. 2. (a) Variation of reflectivity measured on the Al layer. (b) Design of the measurement geometry. (c) SEM image of an AFM probe. Cartographies of the variation of reflectivity performed at two different times [indicated in panel (a) by a green circle and a red lozenge, respectively]: (d) before the peak associated with the longitudinal wave and (e) at the maximum of intensity of the peak. (f) SEM image of a broken AFM probe displaying a defect.

due to the electron-lattice coupling and is referred to as the thermal response. Several peaks can also be observed, the most important peaks being detected at 503, 1014, and 1525 ps. These peaks are caused by an acoustic longitudinal wave bouncing back and forth in the thickness of the cantilever, which modifies the optical properties of the aluminum layer when it is reflected at the free boundary. Reflection at the interface between the Al layer and the silicon may also cause a small change in the profile of those echoes. Given that the speed of sound for longitudinal waves in the silicon along its [100] axis is 8.43×10^3 m s^{-1}, an estimated thickness of the cantilever of 2.14 μm can be calculated from the time between different echoes. This value corresponds well with the values in Table I.

These peaks are detected at the same time at any point of the cantilever with the same thickness. Any thickness variation would result in a different flight time. Thereby, performing a cartography at the exact time of the first peak could be used to reveal thickness variations such as defects and the circular base of the tip. Cartographies performed before and at the time of the maximum of intensity of the peak at 503 ps are shown in Figs. 2(d) and 2(e), respectively. The times are identified on the signal in Fig. 2(a) by a green circle and a red lozenge, respectively. On the first cartography, no structures are observed whereas two disks can be seen on the second one. The first disk (1) corresponds to a defect of the silicon whereas the second (2) indicates the position of the base of the tip. A SEM image of the probe is shown in Fig. 2(f) and these two structures can be observed.

On the map displayed in Fig. 2(d), made before the echo (green dot), we could have expected to observe a thermal

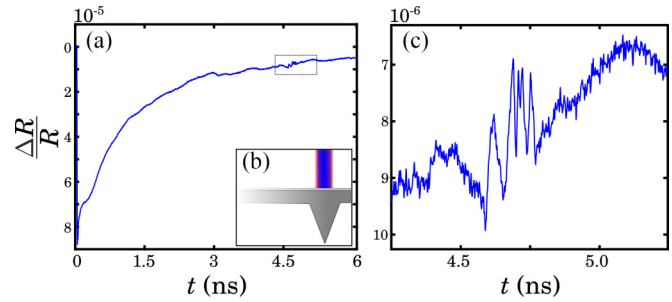

FIG. 3. Variation of reflectivity measured on the aluminum layer measured when both laser beams are focused at the position of the tip on (a) a long temporal window and (c) a short temporal window centered around 4.75 ns in (a) [dotted line in (a)]. (b) Design of the measurement geometry.

signature. However, the thermal diffusion length in the silicon at 1.8 MHz is estimated to be 3.9 μm and does not seem to be large enough to effectively probe the opposite side of the cantilever. A reduction of the modulation frequency could then be necessary to use this discrimination scheme.

The cartography in Fig. 2(e) thereby allows focalization of the pump and probe laser beams just above the apex of the tip in the center of (2) to perform time-resolved measurements. The obtained signal at this position is shown in Fig. 3(a). It displays, similarly to the previous, the signature corresponding to the absorption of the photons and the thermal response of Al. However, the huge peaks corresponding to longitudinal waves in the cantilever are no longer observed. Only a signature of much lower amplitude is detected at a time around 4.5 ns. This echo is due to the reflection of the longitudinal wave emitted after the pump pulse absorption by the aluminum layer and reflected at the end of the tip. The height of the tip is more important than the thickness of the rest of the cantilever, see Table I, and it explains the difference in time and also the amplitude decrease. Still, considering a celerity of 8.43×10^3 m s^{-1}, we can calculate from the flight time of this wave a silicon thickness of 18.9 μm which is coherent with the values given in Table I. This signature is also more complex and reflects a complex reflection mechanism at the end of the tip. None of the transverse waves were experimentally searched over a wider time window, as the amplitude of the longitudinal wave was already close to the noise level. Moreover, in a geometry where the pump and the probe are spatially superimposed, the detection of transverse waves is less sensitive.

The acoustic propagation within the AFM probe has been numerically investigated. A 3D finite element method (FEM) model coded in C++ has been developed. Thereby, the anisotropy of silicon has been taken into account. The acoustic waves are generated by applying a force $F(x, y, t)$ on the top surface

$$F = A \exp\left[-\frac{(x-x_0)^2}{(\sigma_x)^2} - \frac{(y-y_0)^2}{(\sigma_y)^2} - \frac{(t-t_0)^2}{(\sigma_t)^2} \right] \quad (1)$$

with A an arbitrary amplitude, $x_0 = y_0 = 0$ μm the central positions of the function, and $\sigma_x = \sigma_y = 0.25$ μm the half width at half maximum. This spatial variation represents the surface force applied by the absorption of the pump pulse. The

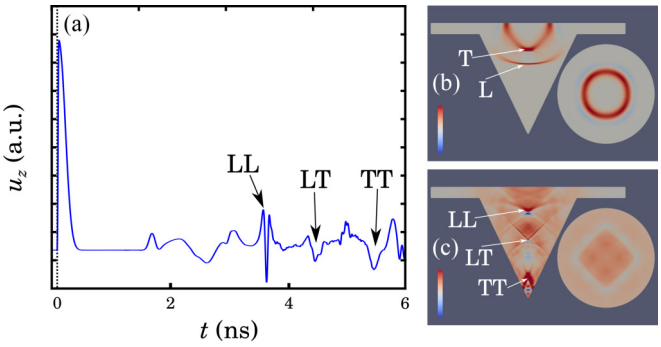

FIG. 4. (a) z component of the displacement calculated at the back of the AFM probe at the center of the tip. Section and top view of the z component of the displacement field in the (001) plane at (b) 0.83 ns and (c) 3.26 ns. The longitudinal and transverse waves are identified L and T, respectively, prior to the reflection at the tip and LL and TT after. The wave identified LT corresponds to a transverse wave obtained by mode conversion from the reflection on the longitudinal wave L.

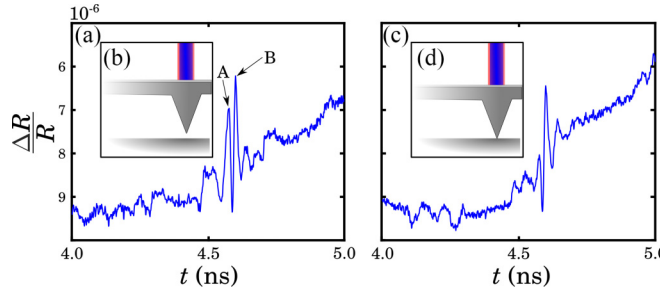

FIG. 5. Variation of reflectivity measured on the Al layer measured when (a) the AFM probe is far from the sample and (c) in contact with a silicon sample. (b) and (d) Designs of the measurement geometries.

time of maximum force is fixed at $t_0 = 0$ ns while $\sigma_t = 10$ ps characterizes its duration. This duration is longer than the experimental laser pulse duration but short enough to be consider an impulsive excitation. The considered density of the silicon is $\rho = 2.33 \times 10^3$ kg/m^3 while the elastic constants are $C_{11} = 165.6$ GPa, $C_{12} = 63.9$ GPa, and $C_{44} = 79.5$ GPa. The propagation of an acoustic pulse is simulated during 6 ns. Figure 4(b) shows an image of the z component of the displacement—along the [100] axis—of the acoustic field within the probe at 0.83 ns in the (001) plane of the silicon. Both a longitudinal and a transverse wave can be identified, respectively, by L and T. Figure 4(c) shows the same field but at a later time, at 3.26 ns, after the reflection at the tip end of the longitudinal wave. Both the longitudinal and the transverse waves can be identified again—now identified LL and TT—as well as an additional transverse wave emitted after the reflection of the longitudinal wave at the edge which is identified as LT. Figure 4(a) introduces the displacement at the center of the tip at position (0, 0, 0) μm. All of the three waves LL, TT, and LT can be identified at 3.65, 5.48, and 4.48 ns, respectively. The arrival times of these waves, in particular the LL wave, are different from the experimental values because the real thickness of the cantilever has not been taken into account in the simulation, in order to reduce the calculation time. The convergence of the exact shape of the echoes between simulation and experiment will be explored in future works. Many phenomena can intervene here such as the attenuation, the exact tip shape, and the frequency content during the generation pulse. As expected, the intensity of the longitudinal wave is much higher than the transverse one. The signature is also less complex than the experimental signal measured which can indicate a much more complex geometry at the edge of the tip than the one considered in this simulation. Moreover, the simulation shows features at shorter times than the LL contribution, which can be attributed to contributions related to the generation of Rayleigh and surface skimming longitudinal waves that are reflected by the edges of the cantilever considered in the geometry. These additional components, that propagate in the back surface of the cantilever, are out of the scope of the present study since we are interested in the acoustic propagation along the tip of the probe.

B. Contact probe sample and surface imaging

Figures 5(a) and 5(c) show the signal measured over a shorter time window centered on the reflected longitudinal echo, when the AFM probe is alone and in contact with a silicon sample. The acoustic experiments require an interferometer, which provides us with a very sensitive means to detect the contact of the tip on the sample surface. For the probe alone, a signature similar to the one shown in Fig. 3 is observed. The slight differences can be attributed to small fluctuations in the exact shape of the tip or to the exact position of the pump and probe beams. This point suggests that future studies on the influence of the shape of the tip on the mechanisms of localization and reflection at the tip could be a focus for optimization. Two important peaks are identified: A and B. When the probe is in contact, a similar signature is observed. However, the amplitude of the peak A is much smaller in this case while the amplitude of peak B remains similar. This can be explained by a change of the boundary conditions at the tip end, and indicates either an acoustic transmission from the probe to the silicon substrate or a modification of the reflection within the probe.

In order to investigate the sensitivity of the signature to the contact force between the probe and the sample, several measurements, shown in Fig. 6, have been performed. Knowing the stiffness constant of the cantilever and the position of the piezoelectric plate on which the sample is mounted, the contact force can be determined. The signals obtained for different force values are displayed in Fig. 6 and exhibit a similar structure with an intensity-reduced peak A. Thereby the observed phenomena is not very sensitive to the contact force between the sample and the probe.

Let us now consider a new sample made of silicon which has been partially covered by a 100 nm gold layer by thermal evaporation, drawn in Fig. 7(b), in order to investigate sensitivity to sample acoustic impedance. In Fig. 7(c), the spatial variation of intensity measured on the AFM probe at two different times is given. It should be noted that both beams as well as the tip are fixed; only the sample is mobile. This

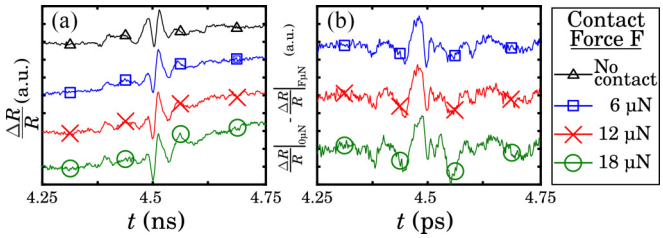

FIG. 6. (a) Comparison of the shape of the reflected echo at the end of the tip as a function of the contact force applied. (b) Subtraction with the noncontact reference. The maximum sensitivity is located on peak A and does not seem to be affected by the quality of the contact. Time $t = 0$ ps is an arbitrary choice and does not correspond to the arrival time of the pump pulse.

way, no guidance system is required and both beams stay focused above the tip during the measurements. The spatial variation of intensity across the step measured at a time before the longitudinal echo shows no clear structure in the signal, only variation due to noise, whereas the variations measured at the time location of peak A show a clear step at 13 μm. The absence of an important step for the measurement performed before the acoustic echo confirms that the step observed on the second signal is not simply due to the height variation of the sample. This first result paves the way to perform surface imaging of a sample displaying Au microstructure obtained by photolithography. An acoustic cartography of the microdisk (1.7 μm radius and 100 nm thickness) is performed and introduced in Fig. 7(d). The profile obtained at the edge

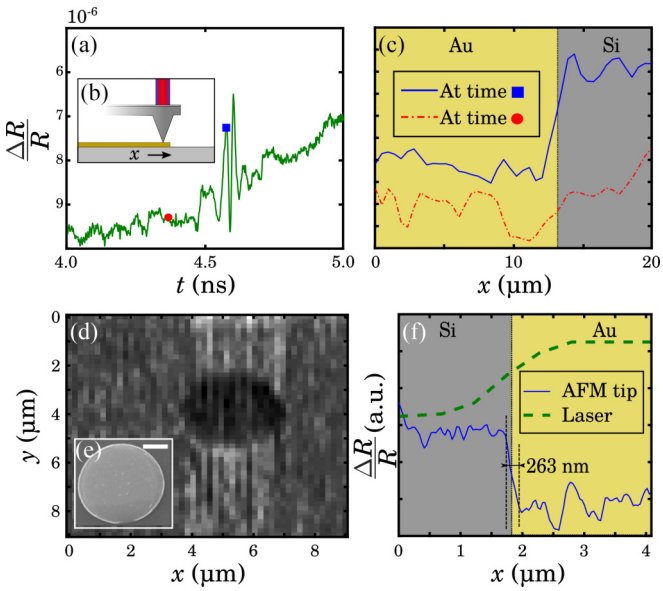

FIG. 7. (a) Variation of reflectivity measured on the Al layer already introduced in Fig. 5(a). (b) Design of the experiment. (c) Spatial variation of reflectivity measured on the Al layer when the AFM tip is in contact with the sample at different times. (d) Cartography obtained through the spatial variation of reflectivity measured on the Al layer revealing the Au structure at the surface of the sample. (e) SEM image of a single disk (white bar is 1 μm). (f) Comparison between the convolution of the plot profile by the probe beam and the acoustic signature measured in the geometry under the AFM tip.

of the disk and displayed in Fig. 7(f) allows the determination a lateral resolution lower than 270 nm. This obtained value is quite far from the expected resolution using a probe with a tip radius of 10 nm. However, an inspection of the probe using a SEM showed that the tip has been slightly blunted with a final radius of the order of 50 nm. Moreover, the apparent resolution is also limited by the steepness of the edges of the lithographed nanostructures which have been estimated at 80 nm. The optical profile of the gold disk obtained by the probe beam is introduced in Fig. 7(f). It is the result of the convolution of the probe beam and the structure profile. The resolution gain is around one order of magnitude.

It should be noted that on the cartography displayed in Fig. 7(d) the intensity measured when the AFM tip is in contact with the Au dot is lower than on the Si substrate. This result is consistent if we consider that the reflection coefficient at the Si/Air interface is of opposite sign to that at the Si/Au interface. Thanks to the use of a piezoelectric stage, the imaging time has been considerably reduced. Here the time to realize the mapping is in the order of 3 minutes.

C. Acoustic transmission

One hypothesis concerning the decrease of the peak A intensity in Fig. 5 is the acoustic transmission from the AFM probe to the sample. In order to confirm or deny this hypothesis, measurements are performed using the transmission experimental setup. The pump beam is still focused on the Al layer covering the AFM probe whereas the probe is focused on the opposite side of the sample which consists of a silicon membrane with a nominal 10 μm thickness; see Fig. 8(d). This sample has been obtained by a chemical wet etching of a SOI silicon wafer in order to obtain a silicon membrane with a normal axis along the [100] axis of the silicon crystal. A thin layer of aluminum has also been deposited on the other side of the sample in order to improve the detection process. The signals measured when the probe and the silicon sample are and are not in contact are introduced in Fig. 8(a). The beginning of the signals does not correspond to the pump pulse absorption. The time window has been deduced from experiments performed without the tip, directly on the membrane, and the flight time in the tip has been added. In the absence of contact, no acoustic waves are detected while in contact an important peak is observed at 359 ps with a full width at half maximum (FWHM) of 15 ± 3 ps. If the probe beam is slightly misaligned with the pump beam, this echo is detected with a slight delay. Thereby, the detection of the peak confirms the acoustic transmission of bulk acoustic wave—in this case the longitudinal wave—through the AFM probe to the sample. The power spectral densities (PSDs) of the signal from Fig. 8(a) are introduced in Fig. 8(b). The PSD of the signal measured in contact gives an estimated highest frequency of 50 GHz. Without contact, the PSD is reasonably flat. The temporal signal in contact in Fig. 8(a) can be well reproduced by a single Gaussian pulse with a FWHM of 15 ps, a maximum of amplitude found at 359 ps, and an offset extracted directly from the experimental signal. The PSD of this theoretical signal also gives a maximum frequency near 50 GHz. However, it is well understood, the generation of

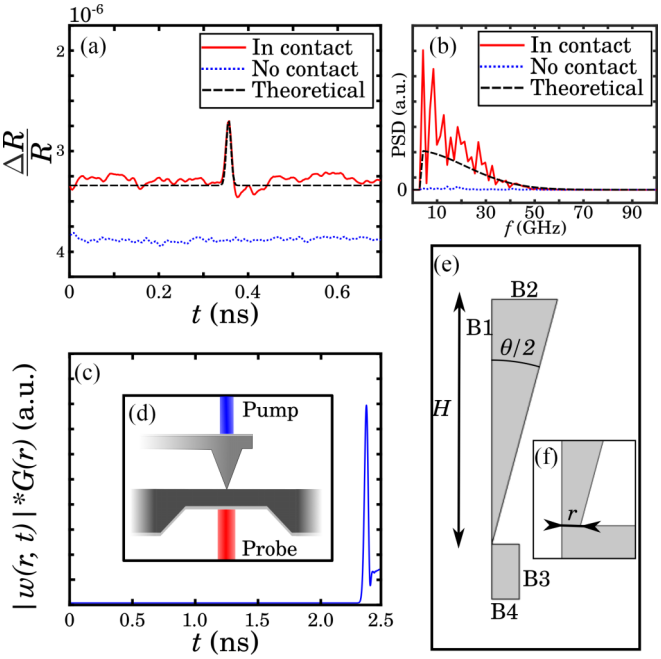

FIG. 8. (a) Transient relative reflectivity measured on the Al layer of the Si membrane when the AFM probe is in contact and not in contact. The time $t = 0$ ps is chosen arbitrarily. Expected signal for a Gaussian pulse centered at 359 ps with a FWHM of 15 ps. (b) Power spectral densities of the signals. (c) Calculated expected signal displaying an important peak at 2.28 ns attributed to the longitudinal wave going through the AFM probe and the membrane silicon. (d) Design of the measurement geometry. (e) Design of the geometry used for the simulation with a zoom (f) on the AFM tip.

frequencies up to hundreds of GHz, using an Al transducer. A possible origin of this frequency filtering could come from attenuation and absorption due to the important thickness of the Si. Another explanation could be the contact between the tip and the sample. One way to improve the coupling is to study the impact of the contact force which in an AFM microscope can be tuned. The shape of the tip itself can also be the cause of this filtering. The wide variety of advanced commercial forms of AFM probe should eventually allow the study and optimization of this transmission. Another way to modify the frequency content of the acoustic waves, and to obtain high frequencies, is to change the optical transducer—the metallic layer on the back of the probe.

The acoustic transmission is also studied numerically using the commercially available software Comsol. Since the acoustic propagation is investigated along a particular axis, the [100] axis of the silicon for both the AFM tip and the silicon membrane, the model can be simplified to reduce calculation costs. Thereby, a temporal study is realized using the Solid Mechanics module and considering a 2D axisymmetry geometry. The geometry, represented in Figs. 8(e) and 8(f), consists of a triangle cut at the end in contact which a rectangular domain corresponding to the silicon membrane. In order to reduce calculation costs, its thickness has been reduced to 4.2 μm. This change is expected to have no consequence on the results except for the acoustic flight time. The domains are considered isotropic, and the mechanical properties are those of the silicon along its [100] axis which are loaded from the material library provided by Comsol. Thereby, the Young's modulus E, the Poisson's ratio ν, and the density ρ considered are respectively $E = 130$ GPa, $\nu = 0.278$, and $\rho = 2.33 \times 10^3$ kg/m^3. A fine mesh, which guarantees a minimum of 5 elements per wavelength for a frequency over 200 GHz for the longitudinal wave, is used. A finer mesh, which has a maximal size of the elements equal to 2 nm, is defined at the tip in order to keep at least 5 elements at the contact surface.

An axial symmetry is applied at the boundary labeled B1 in Fig. 8(e) while a low-reflecting boundary is chosen for the boundary B3. All the other boundaries are free except for the one labeled B2 on which the excitation is applied as a total force expressed by the function $F(r,t)$. The time of maximum force is fixed at $t_0 = 0.1$ ns and the simulation is done for a duration of 2.5 ns with a time step chosen to respect the Courant-Friedrichs-Lewy condition. The rest of the other parameters are unchanged. The simulated signal, expected to be measured in our experimental setup, is obtained by integrating the normal surface displacement at the opposite surface of the membrane, indicated B4 in Fig. 8(e) of the membrane ponderated by the function $G(x)$,

$$G = \exp\left[-\frac{\left(x - x_0^S\right)^2}{\left(\sigma_x^S\right)^2}\right], \tag{2}$$

centered on $x_0^S = 0$ μm and characterized by its width $\sigma_x^S = 0.25$ μm. This function defines the ponderation effect due to the limited size of the probe beam focused on the membrane. None of the Al layers, on top of the AFM probe and covering the other side of the membrane, are taken into account. The calculated signal introduced in Fig. 8(c) displays a single thin peak with a maximum at 2.28 ns. Considering a total silicon thickness of 19.2 μm, this peak can be attributed to a wave propagating with a celerity of 8.43 ms^{-1}. This value is close to the longitudinal speed in silicon along its [100] axis which is 8433 ms^{-1}, calculated from the properties given by the material library of Comsol. This type of simulation predicts an amplitude of the transmitted pulse that is an order of magnitude smaller than the wave that made a round trip through the tip, suggesting that such a pulse can be effectively detected on the opposite side of the membrane. However, it must be noted that the attenuation in the silicon is not taken into account in the simulations. Thereby, the acoustic transmission from the AFM probe to the silicon membrane already observed experimentally is confirmed numerically.

The numerical investigation of the transmission of possible transverse waves from the AFM probe to the membrane has not been performed in this study. Moreover, due to its nanometric radius, the tip of the AFM probe may display a characteristic size smaller than the acoustic wavelength, leading to a complex acoustic transmission phenomena. The influence of the probe shape, especially the tip, is a well-known issue when working with an AFM [49–54]. The details of the transmission will not be discussed here and will be the subject of future work.

IV. CONCLUSION AND PERSPECTIVES

In this paper, we present the results obtained from the study of acoustic propagation in an AFM probe using a picosecond ultrasound technique. The generation of waves in the probe, in particular longitudinal waves, as well as the reflection at its end have been observed experimentally and confirmed numerically. More interestingly, it has been shown that waves reflected at the tip of the probe while it is in contact with a surface allow one to perform impedance mapping with a much better lateral resolution than that obtained by classical optical imaging techniques. The confinement process towards the end of the probe contributes to this reduction of the measurement area. Finally, the acoustic transmission of the AFM probe toward the sample has been demonstrated experimentally and also confirmed numerically. However, it should be emphasized that the lateral resolution remains to be quantified in the transmission mode. Moreover, a possible strong frequency filtering due to the contact would deserve a more specific study in order to quantify it. This frequency cutoff would worsen the resolution of this imaging technique. If the reflection mode seems promising for surface acoustic mapping, the great interest of the transition mode would be to probe small buried structures. In all cases, the sample to be studied will be moved—never the tip—to ensure that the efficiency of the acoustic guidance within the tip does not change. In both modes mentioned here, the measurement of the amplitude and its temporal position can be informative. If successive echoes are detectable, they can be used to locate and size defects or interfaces in depth. These results pave the way for the development of a new acoustic microscopy technique that would enable 3D elastic imaging of the subsurface with nanometric resolution.

ACKNOWLEDGMENT

This work was granted access to the HPC/AI resources of TGCC under the allocation 2021-A0110911930 made by GENCI.

[1] C. Thomsen, J. Strait, Z. Vardeny, H. J. Maris, J. Tauc, and J. J. Hauser, Coherent Phonon Generation and Detection by Picosecond Light Pulses, Phys. Rev. Lett. **53**, 989 (1984).

[2] C. Thomsen, H. T. Grahn, H. J. Maris, and J. Tauc, Surface generation and detection of phonons by picosecond light pulses, Phys. Rev. B **34**, 4129 (1986).

[3] B. Audoin, C. Rossignol, N. Chigarev, M. Ducousso, G. Forget, F. Guillemot, and M. C. Durrieu, Picosecond acoustics in vegetal cells: Non-invasive in vitro measurements at a sub-cell scale, Ultrasonics **50**, 202 (2010).

[4] S. Danworaphong, M. Tomoda, Y. Matsumoto, O. Matsuda, T. Ohashi, H. Watanabe, M. Nagayama, K. Gohara, P. H. Otsuka, and O. B. Wright, Three-dimensional imaging of biological cells with picosecond ultrasonics, Appl. Phys. Lett. **106**, 163701 (2015).

[5] T. Dehoux and B. Audoin, Non-invasive optoacoustic probing of the density and stiffness of single biological cells, J. Appl. Phys. **112**, 124702 (2012).

[6] T. Dehoux, M. A. Ghanem, O. F. Zouani, J.-M. Rampnoux, Y. Guillet, S. Dilhaire, M.-C. Durrieu, and B. Audoin, All-optical broadband ultrasonography of single cells, Sci. Rep. **5**, 8650 (2015).

[7] M. A. Ghanem, A. Khanolkar, H. Zhao, and N. Boechler, Nanocontact tailoring via microlensing enables giant post-fabrication mesoscopic tuning in a self-assembled ultrasonic metamaterial, Adv. Funct. Mater. **30**, 1909217 (2020).

[8] A. Hamraoui, O. Sénépart, M. Schneider, S. Malaquin, E. Péronne, L. Becerra, F. Semprez, C. Legay, and L. Belliard, Correlative imaging of motoneuronal cell elasticity by pump and probe spectroscopy, Biophys. J. **120**, 402 (2021).

[9] J. I. Kilpatrick, I. Revenko, and B. J. Rodriguez, Nanomechanics of cells and biomaterials studied by atomic force microscopy, Adv. Healthc. Mater. **4**, 2456 (2015).

[10] C. Rossignol, N. Chigarev, M. Ducousso, B. Audoin, G. Forget, F. Guillemot, and M. C. Durrieu, *In Vitro* picosecond ultrasonics in a single cell, Appl. Phys. Lett. **93**, 123901 (2008).

[11] M. Khafizov, J. Pakarinen, L. He, H. B. Henderson, M. V. Manuel, A. T. Nelson, B. J. Jaques, D. P. Butt, and D. H. Hurley, Subsurface imaging of grain microstructure using picosecond ultrasonics, Acta Mater. **112**, 209 (2016).

[12] S. Sandeep, T. Thréard, E. De Lima Savi, N. Chigarev, A. Bulou, V. Tournat, A. Zerr, V. E. Gusev, and S. Raetz, 3D characterization of individual grains of coexisting high-pressure H_2O ice phases by time-domain Brillouin scattering, J. Appl. Phys. **130**, 053104 (2021).

[13] T. Thréard, E. de Lima Savi, S. Avanesyan, N. Chigarev, Z. Hua, V. Tournat, V. E. Gusev, D. H. Hurley, and S. Raetz, Photoacoustic 3-D imaging of polycrystalline microstructure improved with transverse acoustic waves, Photoacoustics **23**, 100286 (2021).

[14] K.-H. Lin, C.-M. Lai, C.-C. Pan, J.-I. Chyi, J.-W. Shi, S.-Z. Sun, C.-F. Chang, and C.-K. Sun, Spatial manipulation of nanoacoustic waves with nanoscale spot sizes, Nat. Nanotechnol. **2**, 704 (2007).

[15] H. J. Maris and A. V. Nurmikko, Opto-acoustic methods and apparatus for performing high resolution acoustic imaging and other sample probing and modification operations, U.S. Patent No. US7624640B2 (2009).

[16] H. J. Maris and A. V. Nurmikko, Enhanced ultra-high resolution acoustic microscope, U.S. Patent No. US8302480B2 (2012).

[17] T. Bienville, J. F. Robillard, L. Belliard, I. Roch-Jeune, A. Devos, and B. Perrin, Individual and collective vibrational modes of nanostructures studied by picosecond ultrasonics, Ultrasonics **44**, e1289 (2006).

[18] P. Siry, L. Belliard, and B. Perrin, Picosecond acoustics with very high lateral resolution, Acta Acustica united with Acustica **89**, 925 (2003).

[19] A. Darafsheh, N. I. Limberopoulos, J. S. Derov, D. E. Walker, M. Durska, D. N. Krizhanovskii, D. M. Whittaker, and V. N. Astratov, Optical microscopy with super-resolution by liquid-immersed high-index microspheres, Proc. SPIE **8594**, 85940C (2013).

[20] S. Lee, L. Li, Z. Wang, W. Guo, Y. Yan, and T. Wang, Immersed transparent microsphere magnifying sub-diffraction-limited objects, Appl. Opt. **52**, 7265 (2013).
[21] S. M. Mansfield and G. S. Kino, Solid immersion microscope, Appl. Phys. Lett. **57**, 2615 (1990).
[22] R. Fuentes-Domínguez, F. Pérez-Cota, S. Naznin, R. J. Smith, and M. Clark, Super-resolution imaging using nano-bells, Sci. Rep. **8**, 16373 (2018).
[23] B. Hecht, B. Sick, U. P. Wild, V. Deckert, R. Zenobi, O. J. F. Martin, and D. W. Pohl, Scanning near-field optical microscopy with aperture probes: Fundamentals and applications, J. Chem. Phys. **112**, 7761 (2000).
[24] G. Beane, T. Devkota, B. S. Brown, and G. V. Hartland, Ultrafast measurements of the dynamics of single nanostructures: A review, Rep. Prog. Phys. **82**, 016401 (2018).
[25] A. Crut, P. Maioli, N. Del Fatti, and F. Vallée, Acoustic vibrations of metal nano-objects: Time-domain investigations, Phys. Rep. **549**, 1 (2015).
[26] P.-A. Mante, L. Belliard, and B. Perrin, Acoustic phonons in nanowires probed by ultrafast pump-probe spectroscopy, Nanophotonics-Berlin **7**, 1759 (2018).
[27] W.-S. Chang, F. Wen, D. Chakraborty, M.-N. Su, Y. Zhang, B. Shuang, P. Nordlander, J. E. Sader, N. J. Halas, and S. Link, Tuning the acoustic frequency of a gold nanodisk through its adhesion layer, Nat. Commun. **6**, 7022 (2015).
[28] T. A. Major, A. Crut, B. Gao, S. S. Lo, N. D. Fatti, F. Vallée, and G. V. Hartland, Damping of the acoustic vibrations of a suspended gold nanowire in air and water environments, Phys. Chem. Chem. Phys. **15**, 4169 (2013).
[29] K. Yu, P. Zijlstra, John E. Sader, Qing-H. Xu, and M. Orrit, Damping of acoustic vibrations of immobilized single gold nanorods in different environments, Nano Lett. **13**, 2710 (2013).
[30] D. Chakraborty, G. V. Hartland, M. Pelton, and J. E. Sader, When can the elastic properties of simple liquids be probed using high-frequency nanoparticle vibrations? J. Phys. Chem. C **122**, 13347 (2018).
[31] A. Amziane, L. Belliard, F. Decremps, and B. Perrin, Ultrafast acoustic resonance spectroscopy of gold nanostructures: Towards a generation of tunable transverse waves, Phys. Rev. B **83**, 014102 (2011).
[32] R. Delalande, J. Bonhomme, E. Dandeu, L. Becerra, and L. Belliard, Substrate influence on the vibrational response of gold nanoresonators, Phys. Rev. B **105**, 035422 (2022).
[33] Y. Imade, Vitalyi E. Gusev, O. Matsuda, M. Tomoda, Paul H. Otsuka, and Oliver B. Wright, Gigahertz optomechanical photon-phonon transduction between nanostructure lines, Nano Lett. **21**, 6261 (2021).
[34] C. Jean, L. Belliard, T. W. Cornelius, O. Thomas, Y. Pennec, M. Cassinelli, M. E. Toimil-Molares, and B. Perrin, Spatiotemporal imaging of the acoustic field emitted by a single copper nanowire, Nano Lett. **16**, 6592 (2016).
[35] F. Xu, Y. Guillet, S. Ravaine, and B. Audoin, All-optical in-depth detection of the acoustic wave emitted by a single gold nanorod, Phys. Rev. B **97**, 165412 (2018).
[36] U. Rabe, S. Amelio, E. Kester, V. Scherer, S. Hirsekorn, and W. Arnold, Quantitative determination of contact stiffness using atomic force acoustic microscopy, Ultrasonics **38**, 430 (2000).
[37] U. Rabe, S. Amelio, M. Kopycinska, S. Hirsekorn, M. Kempf, M. Göken, and W. Arnold, Imaging and measurement of local mechanical material properties by atomic force acoustic microscopy, Surf. Interface Anal. **33**, 65 (2002).
[38] U. Rabe and W. Arnold, Acoustic microscopy by atomic force microscopy, Appl. Phys. Lett. **64**, 1493 (1994).
[39] H. J. Sharahi, M. Janmaleki, L. Tetard, S. Kim, H. Sadeghian, and G. J. Verbiest, Acoustic subsurface-atomic force microscopy: Three-dimensional imaging at the nanoscale, J. Appl. Phys. **129**, 030901 (2021).
[40] K. Yamanaka, H. Ogiso, and O. Kolosov, Ultrasonic force microscopy for nanometer resolution subsurface imaging, Appl. Phys. Lett. **64**, 178 (1994).
[41] O. K. Oleg Kolosov and K. Y. K. Yamanaka, Nonlinear detection of ultrasonic vibrations in an atomic force microscope, Jpn. J. Appl. Phys. **32**, L1095 (1993).
[42] U. Rabe, E. Kester, and W. Arnold, Probing linear and nonlinear tip-sample interaction forces by atomic force acoustic microscopy, Surf. Interface Anal. **27**, 386 (1999).
[43] G. J. Verbiest, T. H. Oosterkamp, and M. J. Rost, Subsurface-AFM: Sensitivity to the heterodyne signal, Nanotechnology **24**, 365701 (2013).
[44] G. J. Verbiest and M. J. Rost, Beating beats mixing in heterodyne detection schemes, Nat. Commun. **6**, 6444 (2015).
[45] P. Ahn, Z. Zhang, C. Sun, and O. Balogun, Optical detection of ultrasound using an apertureless near-field scanning optical microscopy system, AIP Conf. Proc. **1511**, 360 (2013).
[46] O. Balogun, Optically detecting acoustic oscillations at the nanoscale: Exploring techniques suitable for studying elastic wave propagation, IEEE Nanotechnology Magazine **13**, 39 (2019).
[47] C. Rossignol, Etude theorique et numerique d'experiences d'acoustique picoseconde, Ph.D. thesis, Universite Pierre et Marie Curie, Paris 6, 2000.
[48] C. Thomsen, H. J. Maris, and J. Tauc, Picosecond acoustics as a non-destructive tool for the characterization of very thin films, Thin Solid Films **154**, 217 (1987).
[49] S. Belikov, N. Erina, L. Huang, C. Su, C. Prater, S. Magonov, V. Ginzburg, B. McIntyre, H. Lakrout, and G. Meyers, Parametrization of atomic force microscopy tip shape models for quantitative nanomechanical measurements, J. Vac. Sci. Technol. **27**, 984 (2009).
[50] L. Calabri, N. Pugno, C. Menozzi, and S. Valeri, AFM nanoindentation: Tip shape and tip radius of curvature effect on the hardness measurement, J. Phys.: Condens. Matter **20**, 474208 (2008).
[51] E. E. Flater, G. E. Zacharakis-Jutz, B. G. Dumba, I. A. White, and C. A. Clifford, Towards easy and reliable AFM tip shape determination using blind tip reconstruction, Ultramicroscopy **146**, 130 (2014).
[52] M. Kopycinska-Müller, R. H. Geiss, and D. C. Hurley, Contact mechanics and tip shape in AFM-based nanomechanical measurements, Ultramicroscopy **106**, 466 (2006).
[53] F. Tian, X. Qian, and J. S. Villarrubia, Blind estimation of general tip shape in AFM imaging, Ultramicroscopy **109**, 44 (2008).
[54] K. L. Westra and D. J. Thomson, Effect of tip shape on surface roughness measurements from atomic force microscopy images of thin films, J. Vac. Sci. Technol. **13**, 344 (1995).